



# Facile synthesis of porous Pt–Pd nanospheres supported on reduced graphene oxide nanosheets for enhanced methanol electrooxidation



Shan-Shan Li <sup>a</sup>, Jing-Jing Lv <sup>b</sup>, Yuan-Yuan Hu <sup>a</sup>, Jie-Ning Zheng <sup>a</sup>, Jian-Rong Chen <sup>b</sup>,  
Ai-Jun Wang <sup>b,\*</sup>, Jiu-Ju Feng <sup>a,\*\*</sup>

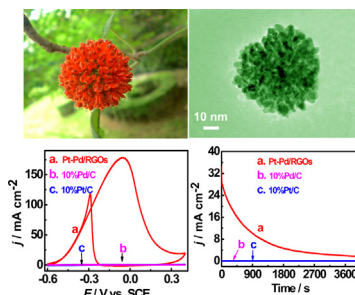
<sup>a</sup> College of Chemistry and Life Science, Zhejiang Normal University, Jinhua 321004, China

<sup>b</sup> College of Geography and Environmental Science, Zhejiang Normal University, Jinhua 321004, China

## HIGHLIGHTS

- Uniform porous Pt–Pd nanospheres supported on reduced graphene oxide were prepared.
- NP-40 was employed as a soft template, without any seed, organic solvent or special apparatus.
- This wet-chemical strategy is simple, facile, and effective.
- The composites exhibit high electrocatalytic activity and long-term stability.

## GRAPHICAL ABSTRACT



## ARTICLE INFO

### Article history:

Received 9 June 2013

Received in revised form

4 August 2013

Accepted 23 August 2013

Available online 2 September 2013

### Keywords:

Reduced graphene oxide nanosheets

Porous nanospheres

Octylphenoxypolye thoxyethanol

Methanol oxidation

Electrocatalysis

## ABSTRACT

In this study, a simple, facile, and effective wet-chemical strategy was developed in the synthesis of uniform porous Pt–Pd nanospheres (Pt–Pd NSs) supported on reduced graphene oxide nanosheets (RGOs) under ambient temperature, where octylphenoxypolye thoxyethanol (NP–40) is used as a soft template, without any seed, organic solvent or special instruments. The as-prepared nanocomposites display enhanced electrocatalytic activity and good stability toward methanol oxidation, compared with commercial Pd/C and Pt/C catalysts. This strategy may open a new route to design and prepare advanced electrocatalysts for fuel cells.

© 2013 Elsevier B.V. All rights reserved.

## 1. Introduction

Fuel cells have been attracting increasing attention in recent decades because of their high efficiency and low/zero emission. Direct methanol fuel cells (DMFCs), using liquid and renewable

methanol fuel, have been considered as a promising candidate in terms of fuel usage and feed strategies [1]. It is known that Pt nanoparticles are thought as the best catalyst in fuel cells, though the Pt-based catalyst still suffers from CO deactivation and its susceptibility to time-dependent drift [2,3]. Furthermore, high cost and limited reserves of Pt in nature are the major obstacle to mass market fuel cells for commercial applications. To realize the commercialization of fuel cells, many efforts are focused on the preparation of economical and effective nanocatalysts, and thereby cost-effective routes are always popular. Thus, different Pt-based

\* Corresponding author.

\*\* Corresponding author. Tel./fax: +86 579 82282273.

E-mail addresses: [ajwangnju@gmail.com](mailto:ajwangnju@gmail.com), [ajwang@zjnu.cn](mailto:ajwang@zjnu.cn) (A.-J. Wang), [jjfeng@zjnu.cn](mailto:jjfeng@zjnu.cn) (J.-J. Feng).

alloyed nanomaterials such as Pt–Ru [4], Pt–Ni [5] and Pt–Co [6] have been prepared to improve the catalytic activity for fuel cells.

In general, surface structure and composition of a catalyst play important roles in determining the catalytic ability, because catalysis reaction is usually occurred on the catalyst surface [7]. Specifically, the surface morphology, size, composition, and crystal structures of a catalyst strongly determine its catalytic efficiency, selectivity, and durability [8,9]. For instance, Liu et al. [10] prepared ring-shaped Pd–Ag nanostructures on graphene nanosheets, which showed improved electrocatalytic activity toward the oxidation of small organic fuels. Moreover, large quantities of atoms located within the interior of solid catalysts are actually not involved in catalysis reaction, because the active sites are only offered by the atoms on the catalyst surface or subsurface. Therefore, porous catalyst with large surface area and more active sites is of great interest, where much less catalyst is required, compared with the solid counterparts.

For the immobilization of catalysts, carbon materials (e.g. carbon black, carbon nanotubes, and nanofibers) are usually used as supports, owing to their high electrical conductivity, high stability, and large surface area [11]. As a new carbon material, graphene has attracted tremendous attention as supports in recent years, because of its large surface area, excellent thermal/chemical stability, high electrical conductivity, and numerous residue oxygen-containing functional groups [12–14]. Up to now, graphene-supported metal nanoparticles are mainly focused on solid mono- and bi-metallic nanocrystals.

Herein, a simple, facile, efficient, and green synthetic approach was developed for the direct preparation of porous Pt–Pd nanospheres (Pt–Pd NSs) uniformly supported on reduced graphene oxide nanosheets (Pt–Pd NSs/RGOs) in aqueous solutions at room temperature, without any seed, organic solvent or hard template. Furthermore, the as-prepared nanocomposites exhibit enhanced catalytic activity toward methanol oxidation, making it promising in fuel cells.

## 2. Experimental

### 2.1. Chemicals and materials

Graphite powder (99.95%, 8000 mesh), commercial 10% Pd/C catalyst, commercial 10% Pt/C catalyst, octylphenoxypolyethoxymethanol (NP-40), formic acid (88%), methanol, chloroplatinic acid ( $\text{H}_2\text{PtCl}_6 \cdot 6\text{H}_2\text{O}$ ) and palladium chloride ( $\text{PdCl}_2$ ) were purchased from Aladdin Chemistry Co. Ltd (Shanghai, China). All the chemicals were used without further purification. All the aqueous solution was prepared with twice-distilled water in the whole experiments.

### 2.2. Catalyst preparation

The graphene oxide nanosheets (GOs) were firstly prepared from natural graphite powder via acid-oxidation based on the modified Hummers method [15,16]. After removal of residual salts and acids, the resultant was further treated by ultrasonication to obtain the exfoliated GOs.

Typical synthesis of the porous Pt–Pd NSs/RGOs was described as follows: the aqueous solution of GOs suspension was ultrasonicated for at least 30 min. Then, 5 mL GOs suspension ( $0.5 \text{ mg mL}^{-1}$ ), 3 mL  $\text{H}_2\text{PtCl}_6 \cdot 6\text{H}_2\text{O}$  (10.0 mM), 3 mL  $\text{PdCl}_2$  (10.0 mM), and 0.5 mL NP-40 ( $0.5 \text{ mg mL}^{-1}$ ) were mixed together into a vial by gentle agitation, followed by the slow addition of 0.5 mL formic acid under stirring. Next, the mixture was kept at room temperature, without disturbance for three days. The resulting black precipitates were collected by centrifugation and

thoroughly washed with water, and finally dried in vacuum at ambient temperature for further characterization.

### 2.3. Characterization

The morphology and crystal structures of the catalysts were characterized by transmission electron microscopy (TEM) and high resolution TEM (HR-TEM) on a JEM-2010F transmission electron microscopy operating at an acceleration voltage of 200 KV equipped with selective area electron diffraction (SAED). The chemical composition was characterized by an energy dispersive X-ray spectroscopy (EDX) with Vantage Digital Acquisition Engine (Thermo Noran, USA). X-ray diffraction (XRD) patterns were obtained on a Rigaku Dmax-2000 diffractometer with a  $\text{Cu K}\alpha$  radiation source ( $\lambda = 0.15418 \text{ nm}$ ). The UV–vis absorption spectra were recorded by using a Lambda950 UV/Vis/NIR spectrometer. The Fourier transform infrared (FT–IR) spectra were recorded with a Nicolet NEXUS670 Fourier transform infrared spectrometer in the wavenumber range of  $500\text{--}4000 \text{ cm}^{-1}$ . X-ray photoelectron spectra were recorded on a K-Alpha XPS spectrometer (ThermoFisher, E. Grinstead, UK) with an Al  $\text{K}\alpha$  X-ray radiation (1486.6 eV) for excitation. Raman spectra of the catalysts were examined by using a Renishaw Raman system model 1000 spectrometer equipped with CCD detector, performed with a He/Ne laser at a wavelength of 633 nm. Thermogravimetric analysis (TGA) was performed on a simultaneous thermo-gravimetric analyzer (NETZSCH STA 449C). The samples were heated under an air atmosphere from room temperature to  $800^\circ\text{C}$  at a rate of  $10^\circ\text{C min}^{-1}$ .

### 2.4. Electrochemical investigation

All the electrochemical measurements were performed at room temperature on a CHI 660D electrochemical workstation (CH Instruments, Chenhua Co., Shanghai, China) with a three-electrode cell configuration. A bare or modified glassy carbon electrode (GCE, 3 mm diameter,  $0.0706 \text{ cm}^2$ ), a platinum wire, and a saturated calomel electrode (SCE) were used as working electrode, counter electrode, and reference electrode, respectively. For the preparation of the Pt–Pd NSs modified electrode, 3 mg of the catalyst was put into 1 mL water and dispersed by ultrasonication for 30 min to obtain a homogeneous suspension. Next, 6  $\mu\text{L}$  of the suspension was uniformly casted on the freshly clean GCE and dried in air. Thus, the specific loading of the catalyst on the electrode surface was  $0.255 \text{ mg cm}^{-2}$ .

The electrochemically active surface area (EASA) of the catalyst was determined by calculating the hydrogen adsorption/desorption area. The charge for monolayer adsorption/desorption of hydrogen on Pt was assumed to be  $210 \mu\text{C cm}^{-2}$ , but it is not rational to derive the EASA of Pt–Pd alloy catalyst from hydrogen region, because hydrogen can diffuse into the Pd bulk to form Pd hydride, instead of adsorbing onto the Pd surface. To evaluate the electrocatalytic activity of the catalysts toward methanol oxidation, voltammetric experiments were performed in a solution containing 1.0 M NaOH and 1.0 M  $\text{CH}_3\text{OH}$  at the scan rate of  $50 \text{ mV s}^{-1}$ .

## 3. Results and discussion

Fig. 1A shows the Pt–Pd NSs uniformly dispersed on the RGOs, with the average diameter of  $52.5 \pm 2.5 \text{ nm}$  based on the particle size histograms (inset in Fig. 1B). The as-prepared products show porous structures (Fig. 1B and C), owing to the essential role of NP-40 as a soft template [17,18]. In addition, a mixed diffraction pattern is observed from the SAED measurements (inset in Fig. 1C), corresponding to (111), (200), (220), and (311) planes from inside to outside. This result is in good accordance with the XRD analysis

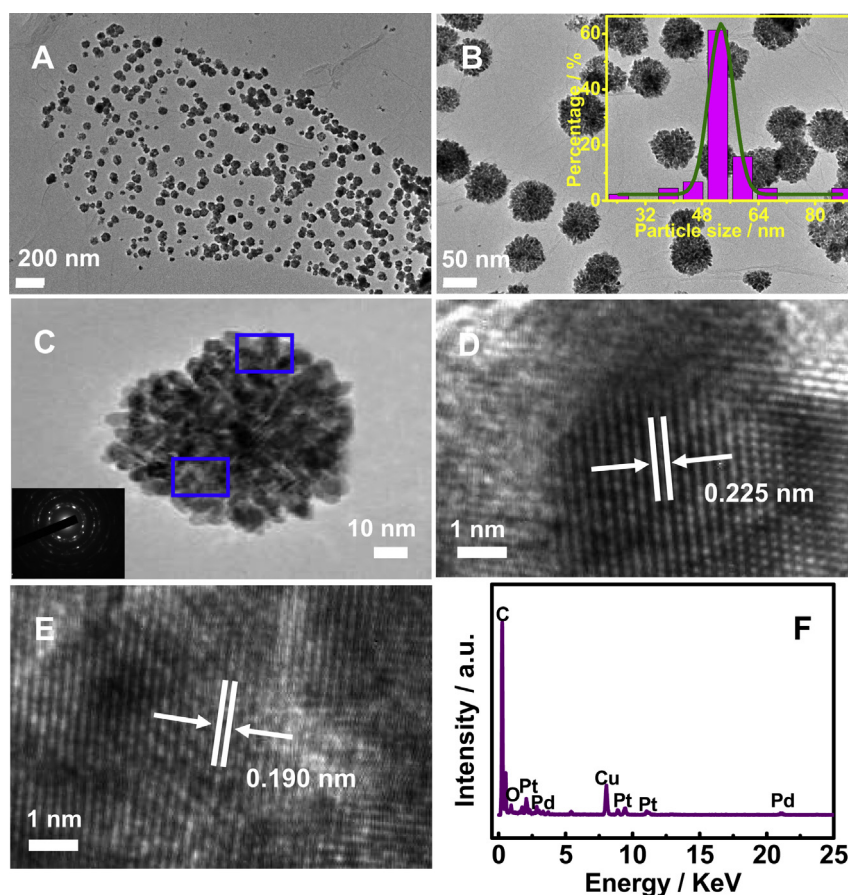


**Fig. 1.** TEM (A) and HR-TEM (B, C, D, E) images of the porous Pt–Pd NSs/RGOs. Inset shows the corresponding particle size distribution (B), SAED (C) and EDX (F) pattern.

(Fig. 3A), suggesting the defects and multiple crystal domains in Pt crystals. Moreover, the HR-TEM images reveal well crystallization of the porous Pt–Pd NSs with a Pt–Pd (111) lattice spacing of 0.225 nm (Fig. 1D). This value is smaller than the lattice spacing of the (111) planes of the face-centered cubic (fcc) Pt and Pd [19]. And a Pt–Pd (200) lattice spacing of 0.190 nm is obtained (Fig. 1E) [20], which agrees well with the value of 0.193 nm calculated by using the (200) diffraction peak based on Debye–Scherrer’s formulation. The measured lattice spacing reflects the expected lattice contraction, which is consistent well with the XRD analysis.

The associated EDX pattern verifies simultaneous existence of Pt and Pd in a single porous Pt–Pd NSs. The atomic ratio of Pt and Pd is ca. 3:1 (Fig. 1F). Furthermore, the elements of C, O, and Cu were also detected. Clearly, the peak of C comes from the RGOs and supporting film of the copper mesh, while the oxygen signal is originated from the incomplete reduction of GOs [21]. Besides, the signals indexed to Cu are attributed to the copper mesh used for the TEM experiments.

As depicted in Fig. 2A, C, D, the peaks located at 71.2, 74.5, 335.4, and 340.8 eV are assigned to the binding energy of Pt  $4f_{7/2}$ , Pt  $4f_{5/2}$ , Pd  $3d_{5/2}$ , and Pd  $3d_{3/2}$ , respectively, revealing the coexistence of Pt and Pd [22]. The elemental component of the porous Pt–Pd NSs/RGOs was listed in Table S1 (Supporting information). The atom ratio of Pt and Pd is about 3:1, which is in accordance with the XPS analysis. Meanwhile, the peak at around 284.5 eV is attributed to the binding energy of C 1s, which was further separated into four peaks at 284.5, 286.6, 287.6, and 288.8 eV (Fig. 2B), corresponding to the C–C ( $sp^2$  C), C–O, C=O, and O–C=O groups, respectively [23,24]. The peaks related to the oxygen functionalities are much weaker, compared with the  $sp^2$  C–C peak, indicating nearly

complete reduction of the GOs. The XPS analysis provides solid support about the synthesis of the porous Pt–Pd NSs/RGOs.

The XRD pattern confirms the formation of the porous Pt–Pd NSs/RGOs (Fig. 3A, curve a), where the representative diffraction peaks at  $40^\circ$ ,  $47^\circ$ ,  $68^\circ$ , and  $82^\circ$  are all in good agreement with the (111), (200), (220) and (311) planes of Pt–Pd alloy [25,26], respectively. However, these diffraction peaks are slightly shifted to higher  $2\theta$  values, compared with the commercial Pt black [27,28], indicating the formation of Pt–Pd alloy. The average lattice parameter value ( $a$ ) is 0.39150 nm, calculated from the four diffraction peaks (Table S2, Supporting information) [29]. Notably, the  $a$  value lies between those of bulk Pt (JCPDS-40-0802 Pt,  $a = 0.39224$  nm) and bulk Pd (JCPDS-46-1043 Pd,  $a = 0.38892$  nm) [27,29], reflecting the lattice contraction for the partial substitution of Pt by Pd. In addition, a broad diffraction peak at  $\sim 23^\circ$  of the sample is indexed to disorderedly stacked graphene [30], different from that of the GOs sample only with a strong peak at  $11^\circ$  that is associated with the (002) planes of GOs (Fig. 3A, curve b). These results indicate the reduction of GOs by formic acid [30].

The formation of the porous Pt–Pd NSs/RGOs was characterized by UV–vis spectroscopy. In the adsorption spectrum of the GOs sample (Fig. 3B, curve b), the adsorption peak at 206 nm can be assigned to the  $\pi$ – $\pi^*$  transitions of aromatic C=C bonds. However, for the porous Pt–Pd NSs/RGOs (Fig. 3B, curve a), a broad peak centered at 282 nm appears, accompanied with the red shift of the adsorption peak at 206 nm–228 nm, suggesting the formation of the RGOs [10,31].

The solid support for GOs reduction is FT–IR spectrum. In the case of the porous Pt–Pd NSs/RGOs (Fig. 3C, curve a), there are

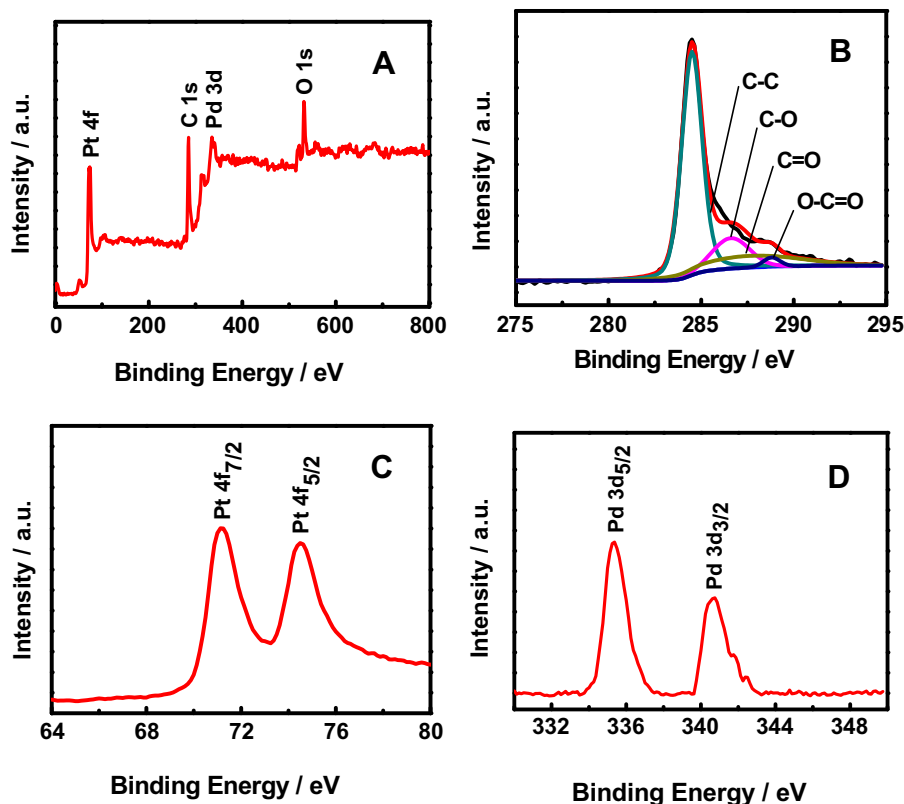


Fig. 2. XPS spectra (A), C 1s XPS spectra (B), the fine spectrum of Pt 4f (C) and Pd 3d (D) of the porous Pt–Pd NSs/RGOs.

three weak peaks and a strong broad one observed at 1060, 1228, 1627, and 3417  $\text{cm}^{-1}$ , which are attributed to the stretching vibration of C–O, stretching vibration of C–OH, skeletal vibration of C=C [24], and O–H stretching vibration of C–OH groups and

water [32], respectively. The observation is quite different from that of the GOs sample (Fig. 3C, curve b), showing almost removal of the oxygen-containing functional groups from the GOs surfaces.

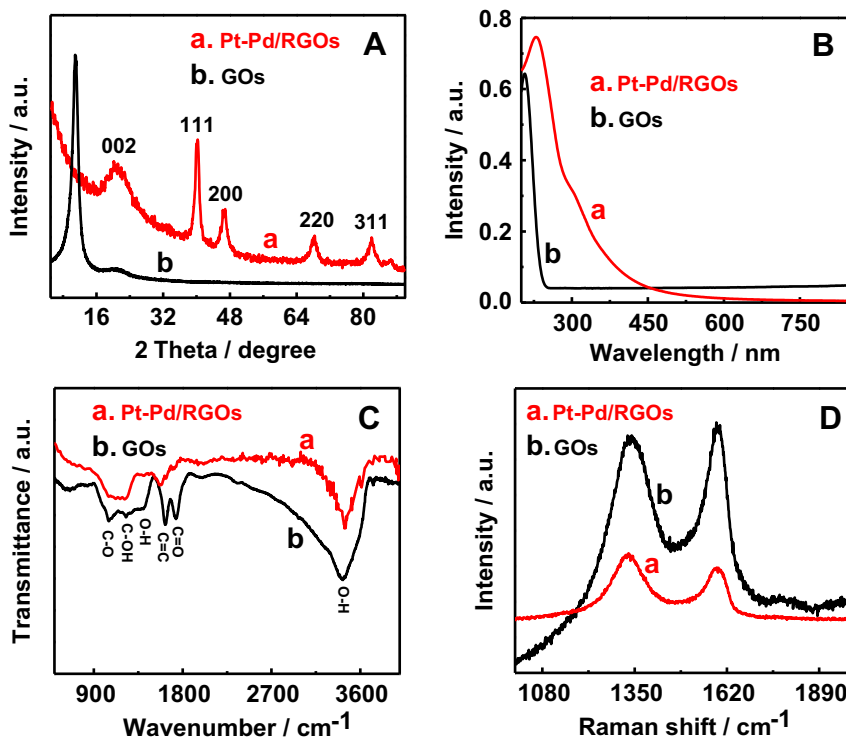


Fig. 3. XRD patterns (A), UV–vis absorption (B), FT–IR (C), and Raman (D) spectra of the porous Pt–Pd NSs/RGOs (curve a) and GOs (curve b), respectively.



Raman spectroscopy is another potent tool to evaluate structural defects, number of layers, and doping level of graphene [33–35]. The typical features for carbon in Raman spectra are the G band corresponding to the doubly degenerate  $E_{2g}$  of graphite [36], while the D band is associated with the  $A_{1g}$  breathing mode of disordered graphite structure [37,38]. Meanwhile, the  $I_D/I_G$  intensity ratio is an indicator of the degree of disorder and average size of the  $sp^2$  domains, evidencing the number of defects in catalysts [36,38,39]. In this study, there are two strong characteristic peaks at  $1351\text{ cm}^{-1}$  for the D band and  $1596\text{ cm}^{-1}$  for the G band for the porous Pt–Pd NSs/RGOs, respectively (Fig. 3D, curve a). As shown, the two bands display a slightly blue shift, compared with the GOs sample (Fig. 3D, curve b). Meanwhile, the  $I_D/I_G$  intensity ratio slightly increases (Table S3, Supporting information), confirming that the highly crystalline structure of graphene was well-preserved even after chemical deposition of Pt–Pd catalysts [19,38]. This is important for achieving good electrical conductivity in the hybrid composites.

TGA analysis was performed to check the weight loss of the porous Pt–Pd NSs/RGOs (Fig. S1, Supporting information). The weight loss below  $100^\circ\text{C}$  is attributed to the escape of water molecules absorbed between the graphene sheets. More importantly, the weight loss is much lower in the temperature range of  $130\text{--}170^\circ\text{C}$ , compared with the GOs sample under the same conditions (curve b), indicating the decrease of the quantity of oxygenated functional groups on the graphene [40,41]. Additionally, the percentage of the porous Pt–Pd NSs by weight is about 88 wt%.

The EASA of the porous Pt–Pd NSs/RGOs modified electrodes is estimated by the CO-stripping measurements (Fig. 4A), assuming a value of  $210\text{ }\mu\text{C cm}^{-2}$  for the oxidation of a CO monolayer [14,31,41,42]

$$\text{EASA}(\text{cm}^2\text{mg}^{-1}) = Q / \{[\text{metal}] \times 210\}$$

Where [metal] represents the loading of Pt and Pd (mg). The EASA of the porous Pt–Pd NSs/RGOs (Fig. 4A) is calculated to be about

$681\text{ cm}^2\text{mg}_{\text{metal}}^{-1}$  (Fig. 4A), which is much larger than that of commercial 10% Pd/C with the value of  $39.4\text{ cm}^2\text{mg}_{\text{metal}}^{-1}$  under identical conditions (Fig. 4B). Furthermore, the onset potential is  $0.516\text{ V}$  for the porous Pt–Pd NSs/RGOs modified electrode, which negatively shifts in comparison with the commercial 10% Pd/C with a value of  $0.593\text{ V}$ , owing to the special structures of the porous Pt–Pd NSs/RGOs.

The electrocatalytic activity of the porous Pt–Pd NSs/RGOs (Fig. 4C, curve a), commercial 10% Pd/C (Fig. 4C, curve b), and 10% Pt/C (Fig. 4C, curve c) modified electrodes was examined by cyclic voltammetry in  $1.0\text{ M NaOH}$  solutions containing  $1.0\text{ M}$  methanol. In each case, a methanol oxidation peak is clearly observed in the forward scan from  $-0.3$  to  $0.0\text{ V}$ . And another anodic peak is detected during the reverse scan, which is associated with the removal of incompletely oxidized carbonaceous species (e.g. CO) formed in the forward scan. In the case of the porous Pt–Pd NSs/RGOs, the maximum forward current density is about  $180\text{ mA cm}^{-2}$ , which is much higher than the commercial 10% Pd/C ( $0.73\text{ mA cm}^{-2}$ ) and 10% Pt/C ( $0.6\text{ mA cm}^{-2}$ ) samples, indicating enhanced catalytic activity of the porous Pt–Pd NSs/RGOs. To evaluate the catalyst tolerance to the CO poisoning, the forward anodic peak current ( $J_F$ ) is compared with the reverse anodic peak current ( $J_R$ ). Herein, the ratio of  $J_F/J_R$  is 1.5 for the porous Pt–Pd NSs/RGOs modified electrodes, which is much bigger than the 20% Pt/C [42] and other similar catalysts [42,43] modified electrodes, demonstrating an increased efficiency in the removal of poisonous CO species from the surface of the catalysts.

Chronoamperometry is used to investigate the electrocatalytic activity and stability of the porous Pt–Pd NSs/RGOs (Fig. 4D, curve a), commercial 10% Pd/C (Fig. 4D, curve b), and commercial 10% Pt/C (Fig. 4D, curve c) modified electrodes using methanol as model molecules at an applied potential of  $-0.3\text{ V}$ . The polarization currents of the porous Pt–Pd NSs/RGOs modified electrode decrease quickly within  $1500\text{ s}$  and then slowly decay above  $3000\text{ s}$  to approach a limiting current (up to  $4000\text{ s}$ ). The initial rapid decay in

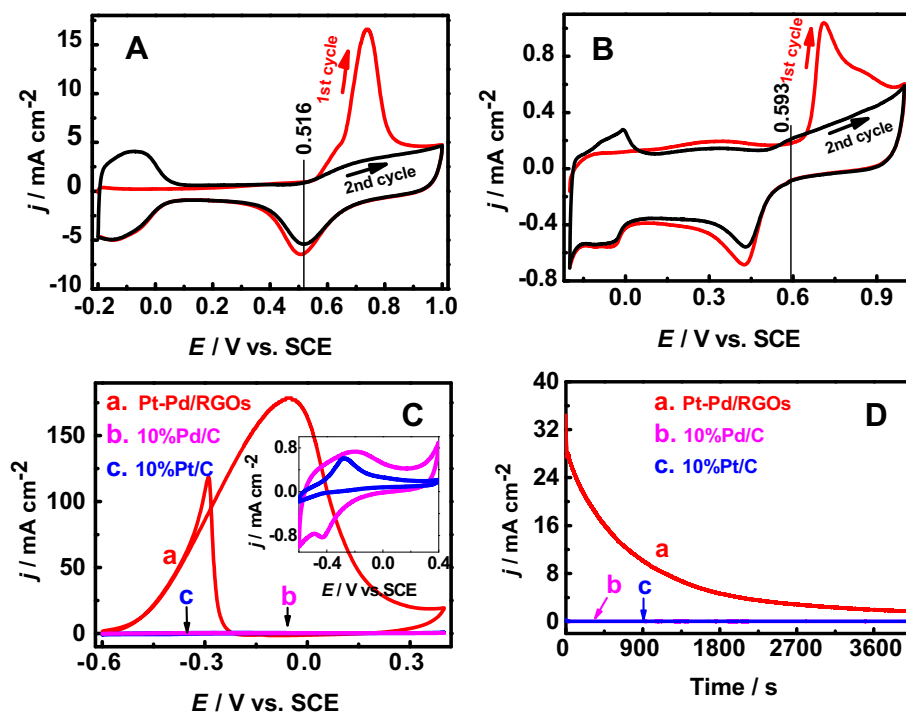


**Fig. 4.** CO-stripping voltammograms of the porous Pt–Pd NSs/RGOs (A) and commercial 10% Pd/C catalyst (B) modified electrodes in  $0.5\text{ M H}_2\text{SO}_4$  at  $50\text{ mV s}^{-1}$ . The CVs (C) recorded at  $50\text{ mV s}^{-1}$  and chronoamperometric curves (D) of the porous Pt–Pd NSs/RGOs (a), commercial 10% Pd/C (b), and commercial 10% Pt/C (c) modified electrodes in  $1.0\text{ M CH}_3\text{OH} + 1.0\text{ M NaOH}$  aqueous solution. Inset shows the corresponding CVs of 10% Pd/C and 10% Pt/C.

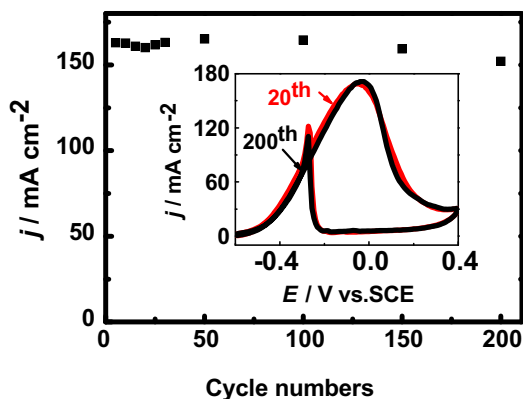


**Fig. 5.** Forward peak current density ( $j_f$ ) as a function of potential scanning cycles of the porous Pt–Pd NSs/RGOs modified electrode in the 1.0 M  $\text{CH}_3\text{OH}$  + 1.0 M NaOH solution. Inset shows the corresponding 20th and 200th CVs of the porous Pt–Pd NSs/RGOs.

current density is ascribed to catalyst poisoning by chemisorbed carbonaceous species such as  $\text{CO}_{\text{ad}}$  formed on the catalysts surface [40,44]. Moreover, the limiting currents of the porous Pt–Pd NSs/RGOs modified electrode decrease to 2.0  $\text{mA cm}^{-2}$  up to 4000 s, much higher than those of the commercial 10% Pd/C (Fig. 4D, curve b) and commercial 10% Pt/C (Fig. 4D, curve c) modified electrodes with a value of nearly zero within 10 s. The satisfactory tolerance, improved electrocatalytic ability and stability of the porous Pt–Pd NSs/RGOs modified electrode are attributed to the special structures of the porous Pt–Pd NSs/RGOs.

The high catalytic activity and excellent stability of the porous Pt–Pd NSs/RGOs modified electrode were further demonstrated by cyclic voltammetry (Fig. 5), where the catalytic current density is almost constant within 200 cycles. For example, using the steady state peak current density of the 20th cycle in the forward scan as a reference, the peak current density on the porous Pt–Pd NSs/RGOs modified electrode remains about 95% after 200 cycles (inset in Fig. 5). The good performance of the porous Pt–Pd NSs/RGOs as a catalyst is possibly due to larger EASA [45], favorable distance between Pt–Pd alloy [46], high load and well-dispersed porous Pt–Pd NSs on RGOs, and good electrical conductivity of graphene.

#### 4. Conclusions

In conclusion, a simple and facile one-pot wet-chemical method was developed for the fabrication of uniform porous Pt–Pd NSs/RGOs, with the assistance of NP-40 as a soft template. The electrochemical experiments show that the as-prepared novel composites have excellent catalytic activity and better stability toward methanol oxidation, making it a promising catalyst in fuel cells. This work provides a new approach in the synthesis of potential porous bimetal/RGOs composites with high catalytic activity.

#### Acknowledgments

This work was financially supported by the NSFC (Nos. 20905021, 21175118, 21275130, and 21275131), the Foundation of the Ministry of Education of China for Returned Scholars (A.J.W. and J.J.F.), preferentially financing projects of scientific and technological activities of overseas students in Zhejiang province (No. [2011]–443, J.-J. Feng).

#### Appendix A. Supplementary data

Supplementary data related to this article can be found at <http://dx.doi.org/10.1016/j.jpowsour.2013.08.088>.

#### References

- [1] A.S. Aricò, S. Srinivasan, V. Antonucci, *Fuel Cells* 1 (2001) 133–161.
- [2] X. Yu, S. Ye, *J. Power Sources* 172 (2007) 145–154.
- [3] L. Qu, Y. Liu, J.-B. Baek, L. Dai, *ACS Nano* 4 (2010) 1321–1326.
- [4] A. Velquez-Palenzuela, F. Centellas, J.A. Garrido, C. Arias, R.M. Rodríguez, E. Brillas, P.-L. Cabot, *J. Power Sources* 196 (2011) 3503–3512.
- [5] B. Habibi, N. Delnavaz, *Int. J. Hydrogen Energy* 36 (2011) 9581–9590.
- [6] W. Trongchuanakij, K. Pruksathorn, M. Hunsom, *Appl. Energy* 88 (2011) 974–980.
- [7] J.-C. Bertolini, *Catal. Today* 138 (2008) 84–96.
- [8] S.E. Habas, H. Lee, V. Radmilovic, G.A. Somorjai, P. Yang, *Nat. Mater.* 6 (2007) 692–697.
- [9] W. Chen, J. Kim, S. Sun, S. Chen, *Langmuir* 23 (2007) 11303–11310.
- [10] M. Liu, Y. W. Chen, *Adv. Funct. Mater.* 23 (2013) 1289–1296.
- [11] B.Y. Xia, B. Wang, H.B. Wu, Z. Liu, X. Wang, X.W. Lou, *J. Mater. Chem.* 22 (2012) 16499–16505.
- [12] M.H. Seo, S.M. Choi, H.J. Kim, W.B. Kim, *Electrochem. Commun.* 13 (2011) 182–185.
- [13] S. Yu, Q. Liu, W. Yang, K. Han, Z. Wang, H. Zhu, *Electrochim. Acta* 94 (2013) 245–251.
- [14] Y. Liu, Y. Huang, Y. Xie, Z. Yang, H. Huang, Q. Zhou, *Chem. Eng. J.* 197 (2012) 80–87.
- [15] W.S. Hummers, R.E. Offeman, *J. Am. Chem. Soc.* 80 (1958), 1339–1339.
- [16] Y. Xu, H. Bai, G. Lu, C. Li, G. Shi, *J. Am. Chem. Soc.* 130 (2008) 5856–5857.
- [17] L. Wang, M. Imura, Y. Yamauchi, *ACS Appl. Mat. Interfaces* 4 (2012) 2865–2869.
- [18] H. Wang, H.Y. Jeong, M. Imura, L. Wang, L. Radhakrishnan, N. Fujita, T. Castle, O. Terasaki, Y. Yamauchi, *J. Am. Chem. Soc.* 133 (2011) 14526–14529.
- [19] W. Qian, R. Hao, J. Zhou, M. Eastman, B.A. Manhat, Q. Sun, A.M. Goforth, J. Jiao, *Carbon* 52 (2013) 595–604.
- [20] X. Huang, Y. Li, Y. Li, H. Zhou, X. Duan, Y. Huang, *Nano Lett.* 12 (2012) 4265–4270.
- [21] L. Dong, R.R.S. Gari, Z. Li, M.M. Craig, S. Hou, *Carbon* 48 (2010) 781–787.
- [22] M. Simoes, S. Baranton, C. Coutanceau, *Appl. Catal. B* 110 (2011) 40–49.
- [23] L. Gao, W. Yue, S. Tao, L. Fan, *Langmuir* 29 (2012) 957–964.
- [24] W. Yue, Z. Lin, S. Jiang, X. Yang, *J. Mater. Chem.* 22 (2012) 16318–16323.
- [25] B. Liu, H.Y. Li, L. Die, X.H. Zhang, Z. Fan, J.H. Chen, *J. Power Sources* 186 (2009) 62–66.
- [26] J. Datta, A. Dutta, M. Biswas, *Electrochem. Commun.* 20 (2012) 56–59.
- [27] G. Fu, K. Wu, J. Lin, Y. Tang, Y. Chen, Y. Zhou, T. Lu, *J. Phys. Chem. C* 117 (2013) 9826–9834.
- [28] T. Lopes, E. Antolini, E.R. Gonzalez, *Int. J. Hydrogen Energy* 33 (2008) 5563–5570.
- [29] D.G. Narehood, S. Kishore, H. Goto, J.H. Adair, J.A. Nelson, H.R. Gutierrez, P.C. Eklund, *Int. J. Hydrogen Energy* 34 (2009) 952–960.
- [30] S. Pei, J. Zhao, J. Du, W. Ren, H.-M. Cheng, *Carbon* 48 (2010) 4466–4474.
- [31] Y. Lu, Y. Jiang, H. Wu, W. Chen, *J. Phys. Chem. C* 117 (2013) 2926–2938.
- [32] N.I. Kovtyukhova, P.J. Ollivier, B.R. Martin, T.E. Mallouk, S.A. Chizhik, E.V. Buzaneva, A.D. Gorchinskiy, *Chem. Mater.* 11 (1999) 771–778.
- [33] T. Hu, J. Zhou, J. Dong, *Phys. Lett. A* 377 (2013) 399–404.
- [34] T.V. Cuong, V.H. Pham, Q.T. Tran, S.H. Hahn, J.S. Chung, E.W. Shin, E.J. Kim, *Mater. Lett.* 64 (2010) 399–401.
- [35] A.C. Ferrari, *Solid State Commun.* 143 (2007) 47–57.
- [36] C. Hu, Y. Cao, L. Yang, Z. Bai, Y. Guo, K. Wang, P. Xu, J. Zhou, *Appl. Surf. Sci.* 257 (2011) 7968–7974.
- [37] X. An, F. Liu, Y.J. Jung, S. Kar, *J. Phys. Chem. C* 116 (2012) 16412–16420.
- [38] A.C. Ferrari, J.C. Meyer, V. Scardaci, C. Casiraghi, M. Lazzeri, F. Mauri, S. Piscanec, D. Jiang, K.S. Novoselov, S. Roth, A.K. Geim, *Phys. Rev. Lett.* 97 (2006) 187401.
- [39] E. Antolini, J.R.C. Salgado, E.R. Gonzalez, *Appl. Catal. B* 63 (2006) 137–149.
- [40] J.-D. Qiu, G.-C. Wang, R.-P. Liang, X.-H. Xia, H.-W. Yu, *J. Phys. Chem. C* 115 (2011) 15639–15645.
- [41] S. Sharma, A. Ganguly, P. Papakonstantinou, X. Miao, M. Li, J.L. Hutchison, M. Delichatsios, S. Ukleja, *J. Phys. Chem. C* 114 (2010) 19459–19466.
- [42] C. Hu, H. Cheng, Y. Zhao, Y. Hu, Y. Liu, L. Dai, L. Qu, *Adv. Mater.* 24 (2012) 5493–5498.
- [43] C. Hu, Y. Guo, Y. Cao, L. Yang, Z. Bai, K. Wang, P. Xu, J. Zhou, *Mater. Sci. Eng. B* 176 (2011) 1467–1473.
- [44] H. Zhang, X. Xu, P. Gu, C. Li, P. Wu, C. Cai, *Electrochim. Acta* 56 (2011) 7064–7070.
- [45] A. Sarkar, A.V. Murugan, A. Manthiram, *Langmuir* 26 (2009) 2894–2903.
- [46] X. Li, X. Wang, S. Song, D. Liu, H. Zhang, *Chem. Eur. J.* 18 (2012) 7601–7607.